ACS APPLIED MATERIALS & INTERFACES

www.acsami.org

Research Article

Opposite Polarity Surface Photovoltage of MoS_2 Monolayers on Au Nanodot versus Nanohole Arrays

Jungeun Song, Soyeong Kwon, Bora Kim, Eunah Kim, Lakshmi N. S. Murthy, Taejin Lee, Inhae Hong, Byoung Hoon Lee, Sang Wook Lee, Soo Ho Choi, Ki Kang Kim, Chang-Hee Cho, Julia W. P. Hsu, and Dong-Wook Kim*

Cite This: https://dx.doi.org/10.1021/acsami.0c14563

Read Online

ACCESS | Metrics & More | Article Recommendations | Supporting Information

ABSTRACT: We prepared MoS_2 monolayers on Au nanodot (ND) and nanohole (NH) arrays. Both these sample arrays exhibited enhanced photoluminescence intensity compared with that of a bare SiO_2/Si substrate. The reflectance spectra of MoS_2/ND and MoS_2/NH had clear features originating from excitation of localized surface plasmon and propagating surface plasmon polaritons. Notably, the surface photovoltages (SPV) of these hybrid plasmonic nanostructures had opposite polarities, indicating negative and positive charging at MoS_2/ND and MoS_2/NH, respectively. Surface potential maps, obtained by Kelvin probe force microscopy, suggested that the potential gradient led to a distinct spatial distribution of photo-generated charges in these two samples under illumination. Furthermore, the local density of photo-generated excitons, as predicted from optical simulations, explained the SPV spectra of MoS_2/ND and MoS_2/NH. We show that the geometric configuration of the plasmonic nanostructures modified the polarity of photo-generated excess charges in MoS_2. These findings point to a useful means of optimizing optoelectronic characteristics and improving the performance of MoS_2-based plasmonic devices.

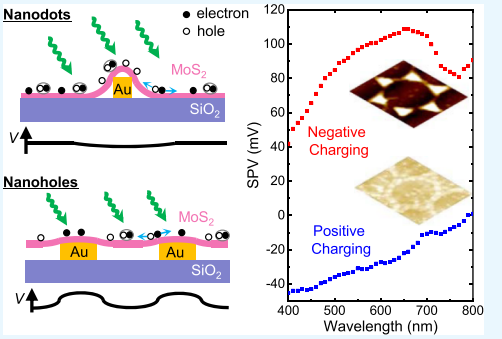

KEYWORDS: *MoS_2, localized surface plasmon, surface plasmon polariton, photoluminescence, surface photovoltage*

INTRODUCTION

The unique physical phenomena occurring in hybrid systems consisting of transition metal dichalcogenide (TMD) materials and metal nanostructures have received considerable research attention.[1−13] In TMD/metal hybrid systems, excitation of surface plasmons not only provides a means of overcoming the limitations of light−matter interactions but also enables tuning of the spectral response of TMD materials.[1−11] Thus, integration of plasmonic nanostructures can improve the performance of TMD-based devices for various applications, such as catalysis, sensing, light-emitting devices, and photovoltaics.[1−3]

Localized surface plasmons (LSPs) give rise to strong light confinement near metal nanostructures. LSP effects can markedly enhance optical absorption and emission in TMD layers on and under metal nanostructures.[4−7] Propagating surface plasmon polaritons (SPPs) along the metal/dielectric interface can also tune the optical characteristics of TMD layers.[8−11] Many researchers have revealed differences between the features of SPPs and those of LSPs in metal/TMD hybrid systems, including selective creation of specific excitons, strong exciton−plasmon coupling, and ultrafast transfer of hot electrons at the TMD/metal interface.[8−11]

Nanosphere lithography (NSL) has notable advantages as a low-cost and high-throughput nanopatterning technique.[14−17] There have been numerous NSL-based studies on the use of close-packed polystyrene (PS) beads as a shadow mask to fabricate hexagonal arrays of nanodots (NDs) through. In addition, etching of PS beads followed by metal deposition enables fabrication of nanohole (NH) arrays.[16,17] Metal ND arrays support LSP resonance, which have a spectral response that is mainly determined by dielectric functions of the metal and the geometry of the individual ND. Arrays of NHs in a metal film allow both the SPP and LSP modes to couple to incoming light. Plasmon−exciton coupling, mediated by both LSP and SPP contributions, provides us with the opportunity to better understand the rich physics of TMD/metal hybrid nanostructures.

Contact potential difference (CPD) in the dark is determined by [(work function of a sample) − (work function of a probe)]/|e| (*e*: the electron charge).[13,18−21] CPD measurements are a versatile technique for characterizing

Received: August 15, 2020
Accepted: October 1, 2020

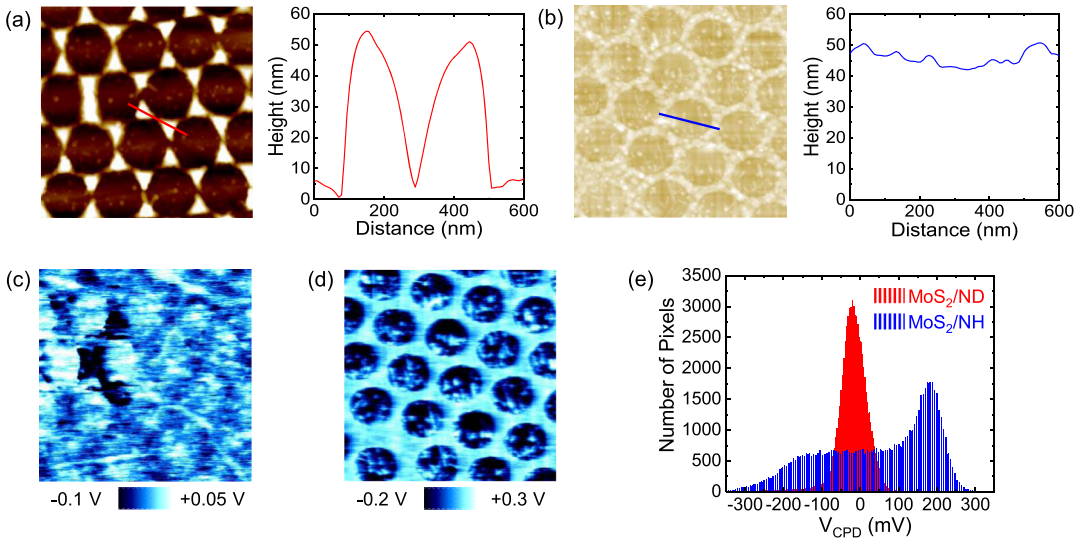

Figure 1. AFM images and height profiles of (a) MoS_2/ND and (b) MoS_2/NH. (c,d) Maps and (e) histograms of CPD_D obtained from the same region in a and b. Total area of the AFM images and CPD_D maps is 2 × 2 μm^2.

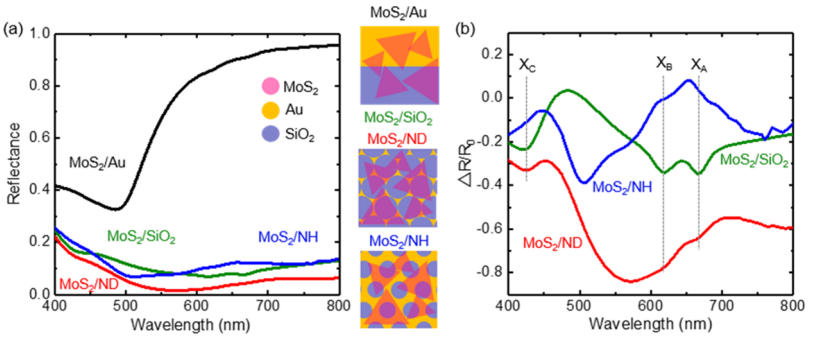

Figure 2. (a) Reflectance and (b) differential reflectance spectra of MoS_2/SiO_2 (green), MoS_2/Au (black), MoS_2/ND (red), and MoS_2/NH (blue). (a) Schematic illustrations of the four sample types. X_A, X_B, and X_C indicated by dashed lines represent A, B, and C excitons in MoS_2 monolayers, respectively.

semiconductor materials and their devices.[6,13,18−21] For example, dopant concentrations of semiconductors, band bending at semiconductor junctions, and electric dipole layers at interfaces can be measured through CPD.[13,18] A potential gradient and/or band offset can modify the spatial distribution of photo-generated charges. The resulting CPD change is called surface photovoltage (SPV).[6,19−21] The SPV is defined as $[CPD_D - CPD_L]$, where CPD_D and CPD_L are CPD measured in the dark and under light illumination, respectively. The polarity and density of excess charges determine the sign and magnitude of a SPV signal.[19−21] SPV characterization can reveal the influence of light illumination on charge dynamics in a variety of semiconductor materials. Moreover, optical and SPV spectra can be compared to probe defect states in semiconductor materials and their optoelectronic devices.[21]

In this work, MoS_2 monolayer flakes were transferred onto the Au ND and NH arrays fabricated by NSL techniques. Contributions of plasmonic effects were apparent in the optical characterization of the MoS_2/ND and MoS_2/NH samples. In addition, measured CPD maps and SPV spectra, which directly depend on the net charges at the surface, provide us opportunities to unveil photon−plasmon−exciton coupling phenomena in our MoS_2/Au hybrid nanostructures.

RESULTS AND DISCUSSION

Figure 1a,b shows atomic force microscopy (AFM) images and height profiles of the MoS_2 flakes transferred onto the ND and NH patterns, respectively. The ND pattern consists of triangular-shaped Au NDs with hexagonal symmetry. The NH pattern is a continuous Au thin film with an array of NHs (diameter: 400 nm). The peak-to-valley heights for both MoS_2/ND and MoS_2/NH were almost the same as the thickness of the Au(50 nm)/Ti(3 nm) film (Figure S1, Supporting Information). The thickness of the metal layer is similar to those used in other TMD/metal nanostructures.[4,5] As shown in Figure 1a, a large portion of the MoS_2 flakes in MoS_2/ND contacted the SiO_2 surface except for a limited region close to the Au NDs. In MoS_2/NH, the MoS_2 flakes were suspended over the NHs (Figure 1b). The morphology of the MoS_2 layers could be determined by the distinct geometric configuration of the ND and NH patterns since the fabrication procedures for the two samples were identical.

The CPD_D maps of the MoS_2 flakes on the ND and NH patterns, obtained by Kelvin probe force microscopy (KPFM), are shown in Figure 1c,d, respectively. In MoS_2/ND, the measured CPD_D near the NDs was negative but that at the SiO_2 surface was positive. MoS_2/NH had much clearer CPD_D contrast, compared with that of MoS_2/ND. This suggests that the electronic interaction at the MoS_2/Au contact rather than

https://dx.doi.org/10.1021/acsami.0c14563
ACS Appl. Mater. Interfaces XXXX, XXX, XXX−XXX

the ND-induced local strain dominantly affected the CPD_D maps of MoS_2/ND.[12,13] The CPD_D of the suspended MoS_2 region was negative, whereas that of the MoS_2 on the Au layer was positive. At the MoS_2/Au contact, charge redistribution can modify the carrier concentration in MoS_2 and increases CPD_D of MoS_2.[13] The CPD_D difference in MoS_2/NH clearly visualizes such strong electronic interactions.

The histogram in Figure 1e shows the CPD_D distributions in MoS_2/ND and MoS_2/NH. MoS_2/NH had a more pronounced CPD_D contrast than that of the MoS_2/ND, as expected from their CPD_D maps (Figure 1c,d). The maximum magnitude of the measured CPD_D in MoS_2/ND was less than 100 mV, whereas that of the MoS_2/NH was greater than 200 mV. The MoS_2 region on the Au layer in MoS_2/NH had the largest positive CPD_D, and the suspended MoS_2 region in MoS_2/NH had the smallest negative CPD_D. The local CPD and its variation respectively reflect the electric potential and electric field (i.e., the potential gradient) at a specific location.[6] In MoS_2/ND, electrons tend to move toward the MoS_2 region on the SiO_2 surface for positive CPD and holes move toward the Au NDs for negative CPD. In MoS_2/NH, electrons and holes move toward the MoS_2 region on the Au layer for positive CPD and the suspended MoS_2 region for negative CPD. These differences should be considered to understand the behaviors of excess charges in the hybrid nanostructures under light illumination.

Figure 2a shows reflectance (R) spectra of MoS_2/ND, MoS_2/NH, and MoS_2 monolayer flakes on a flat 50 nm thick Au thin film (MoS_2/Au) and MoS_2 monolayer flakes on a SiO_2/Si substrate (MoS_2/SiO_2). MoS_2/Au had a much larger R value than the other samples, and the spectrum was similar to that of a bare Au thin film (Figure S2a, Supporting Information). As shown in Figure 2a, both the Au nanopatterns gave a lower R value than that with a 100 nm SiO_2/Si substrate, and MoS_2/ND had the smallest R among all measured samples (see Figure S2a,b, Supporting Information). Figure 2b had a differential reflectance, $\Delta R/R_0$, defined as $(R - R_0)/R_0$, where R and R_0 are the reflectance of the sample and a bare SiO_2/Si substrate, respectively. The SiO_2/Si substrate does not exhibit destructive interference in the wavelength (λ) range from 400 to 800 nm (Figure S2a, Supporting Information) because the optical path difference of the 100 nm-thick SiO_2 layer is small.[23] The $\Delta R/R_0$ spectrum of the MoS_2/SiO_2 (Figure 2b) had local minima at λ = 665, 620, and 440 nm, which originate from the A, B, and C excitonic resonances, respectively (also see Figure S2b, Supporting Information).[24] Features of such excitons also appeared in the spectra of MoS_2/SiO_2, MoS_2/ND, and MoS_2/NH, as indicated by the dashed lines in Figure 2b. The measured spectra of the bare samples were compared with those obtained by numerical calculations (Figure S2a, Supporting Information). Good agreement between them suggested that the defects in the NSL-fabricated nanopatterns did not significantly affect their optical spectra in the visible wavelength range, as reported by Jensen et al.'s work.[14]

The reflectance spectra strongly depended on the geometric configuration of the Au nanopatterns. The $\Delta R/R_0$ value of MoS_2/ND was less than −0.5 at λ > 500 nm and had a minimum at $\lambda \approx$ 570 nm (Figure 2b). This marked reduction of R is attributed to enhanced optical absorption in the MoS_2 layers through LSP excitation. Also, the absorption in the Au NDs and the underlying Si substrates is increased, as shown in the notable antireflection effects of the bare ND sample (Figure S2a, Supporting Information). Conversely, MoS_2/NH did not have any notable anti-reflection effects compared with MoS_2/SiO_2. The $\Delta R/R_0$ value of MoS_2/NH had local minima at $\lambda \approx$ 520 and 730 nm, which are attributed to excitation of SPPs and LSPs.[14]

Angle-resolved differential reflectance spectra of MoS_2/ND and MoS_2/NH are shown in Figure 3a,b, respectively. The

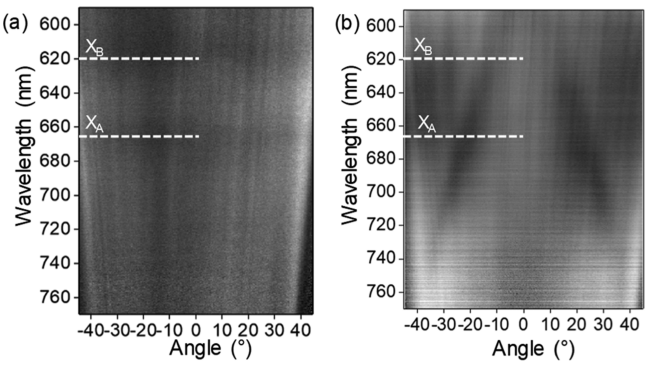

Figure 3. Angle-resolved differential reflectance spectra of (a) MoS_2/ND and (b) MoS_2/NH. X_A and X_B indicated by dashed lines represent A and B excitons of MoS_2 monolayers, respectively.

measurements were performed using a home-built angle-resolved microscopy setup.[25] The reflectance of the Au thin film was selected as a reference to calculate the differential reflectance of the sample to clarify the roles of the nanopatterns. MoS_2/ND did not show any noticeable angle dependence, whereas MoS_2/NH featured dips and a red-shift at wider angles. The clear angle dependence of the MoS_2/NH is attributed to the dispersion relation of the SPP mode, which is supported by the periodic Au NH.[15] Furthermore, somewhat weak dips appeared at 665 and 620 nm, originating from A and B exciton states in MoS_2 (labeled as X_A and X_B in Figure 3), respectively.[24] The SPP-exciton coupling in MoS_2/NH is in the weak coupling regime, and anti-crossing cannot be seen in the reflectance spectrum. The SPP mode wavelengths are close to the exciton resonance wavelengths; hence, SPP-exciton coupling is expected in MoS_2/NH.

Figure 4 shows photoluminescence (PL) spectra of MoS_2/Au, MoS_2/SiO_2, MoS_2/ND, and MoS_2/NH. MoS_2/Au exhibited much weaker PL intensity than that of the other samples. Such PL quenching has been explained by charge transfer at the MoS_2/Au interface and resulting suppression of the radiative recombination of photo-generated excitons.[6,13] The PL intensity of MoS_2/NH and MoS_2/ND was

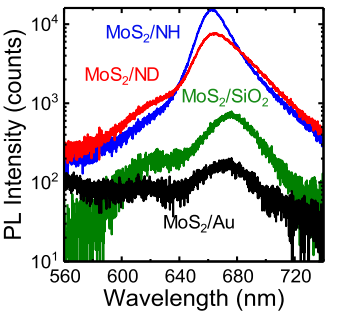

Figure 4. PL spectra of MoS_2/Au (black), MoS_2/SiO_2 (green), MoS_2/ND (red), and MoS_2/NH (blue).

https://dx.doi.org/10.1021/acsami.0c14563
ACS Appl. Mater. Interfaces XXXX, XXX, XXX−XXX

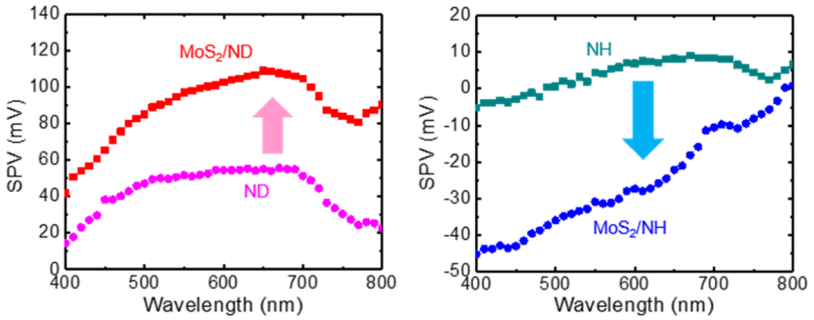

Figure 5. SPV spectra of a bare ND (magenta), MoS_2/ND (red), a bare NH (cyan), and MoS_2/NH (blue) in the visible wavelength range.

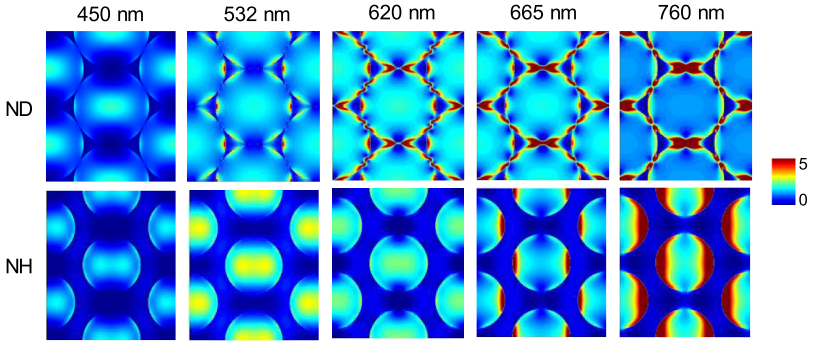

Figure 6. Calculated electric field intensity distributions of ND and NH under illumination of light with λ = 450, 532, 620, 665, and 760 nm.

considerably enhanced, although the samples had an Au layer. The enhanced PL intensity of both MoS_2/NH and MoS_2/ND suggested that plasmonic enhancement of excitation and emission efficiency can exceed the nonradiative processes at the MoS_2/Au interface. The strong and weak PL intensity peaks, as shown in Figure 4, originate from the A and B excitons, respectively.[24] The PL spectra were measured with the use of a micrometer-sized laser beam from several different locations of each sample. The measured PL intensity varied depending on the location, owing to the nonuniformity of the MoS_2 layers and nanopatterns.[14−17] The PL spectra in Figure 4 show the greatest peak intensities of each sample, which reflect that the signals measured from other regions also had a similar tendency. The PL spectra revealed that the peak position shifted depending on the underlying layer. Neutral excitons typically have larger binding energies than those of charged excitons.[24] Charge transfer from a metallic surface and/or trapped charges at the MoS_2/dielectric interface can change the carrier concentration of MoS_2.[6,13] Hence, the doping level in MoS_2 can affect the relative population of neutral and charged excitons, causing the PL peak to shift.[24]

Figure 5 shows SPV spectra of (left) ND and MoS_2/ND, and (right) NH and MoS_2/NH samples with respect to the reference Au probe in the dark steady-state. The SPV signals are the averages over the 2 mm diameter probe area. Both the NH and ND samples without MoS_2 had a relatively small positive SPV across the measured wavelength range. Positive (negative) SPV signals revealed the accumulation of electrons (holes) at the surface.[19−21] Downward band bending occurred at the interface of the SiO_2 and p-type Si; hence, photogenerated electrons (holes) moved toward (away from) the surface during light illumination. Consequently, band bending became less severe, leading to the SPV becoming more positive.[26] The magnitude of the SPV measured from a bare SiO_2/Si substrate was as great as 300−400 mV in the visible wavelength range (Figure S3, Supporting Information). Metal thin films cannot support either accumulation or depletion of electrons under light illumination, owing to the large number of free electrons. Thus, the SPV signals were considerably reduced for the MoS_2 on Au films (Figure S3, Supporting Information). The surface plasmon excitation markedly increased the absorption and scattering cross-section of the Au nanostructures.[4−12] Such plasmonic effects and shadowing effects of the Au nonpatterns reduced optical absorption in the exposed SiO_2/Si region. As a result, the ND and NH samples exhibited a small positive SPV compared with that of the bare SiO_2/Si substrates (Figure S3, Supporting Information).

The SPV signals measured from MoS_2/ND and MoS_2/NH were of greater magnitude than those from the bare ND and NH samples (Figure 5). Clearly, photo-generated charge carriers in the MoS_2 monolayers contributed to this difference. Notably, the SPV signals of MoS_2/ND and MoS_2/NH had opposite polarity across the measured wavelength range: [SPV of MoS_2/ND] > 0 and [SPV of MoS_2/NH] < 0 (Figure 5). Thus, positive and negative charging occurred at the MoS_2 surface of MoS_2/NH and MoS_2/ND, respectively. In addition, the SPV spectra of MoS_2/ND and MoS_2/NH had distinct behaviors in their wavelength dependence: the magnitude of the SPV for the former had a maximum at $\lambda \approx 650$ nm, whereas that of the latter decreased as the wavelength increased.

The top-view electric field intensity maps for ND and NH, under illumination of light with λ = 450, 532, 620, 665, and 760 nm, are shown in Figure 6. The simulation was performed using the finite difference time domain method (Lumerical Solutions) with a normally incident plane wave light source. The optical constants of Si, SiO_2, Ti, and Au were taken from the literature.[27,28] The electric field intensity was estimated at 20 nm above the SiO_2 surface. At $\lambda \geq 532$ nm, the electric field intensified at the edge of the Au NDs. LSP excitation

https://dx.doi.org/10.1021/acsami.0c14563
ACS Appl. Mater. Interfaces XXXX, XXX, XXX−XXX

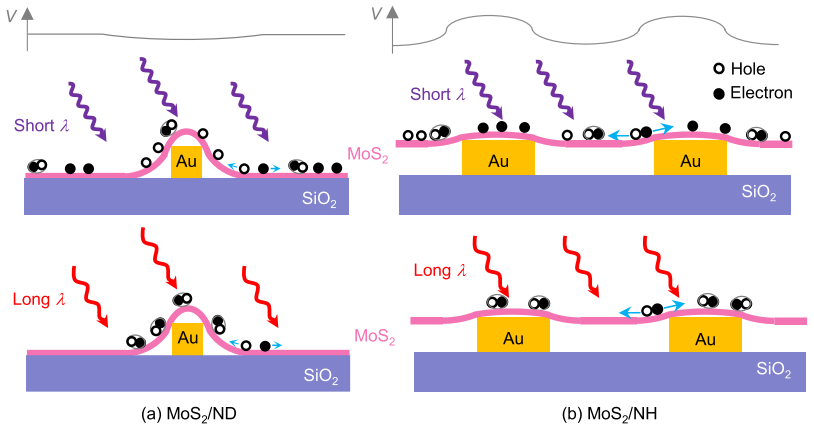

Figure 7. Schematic illustrations of electric potential (V) distributions (top) and expected behaviors of photo-generated excitons and charge carriers in (a) MoS_2/ND and (b) MoS_2/NH at short and long wavelengths (bottom). Blue arrows indicate drift motion of charges.

concentrated incident light near the NDs leading to broadband antireflection effects, as shown in the R and $\Delta R/R_0$ spectra of MoS_2/ND (Figure 2a,b).[14−17] The map of NH at λ = 532 nm clearly showed a large electric field near the center of the holes. Such a strong field should enhance absorption in the MoS_2 monolayer, resulting in a negative $\Delta R/R_0$ of MoS_2/NH, as shown in the $\Delta R/R_0$ spectrum (Figure 2b). A large field in the middle of the NHs in Au and Ag thin films has been reported in earlier works and explained by radial propagation and interference of SPPs from adjacent NHs.[29,30] The electric field intensity near the edge of the Au layer was strong for the NH sample at λ = 665 and 760 nm, where $\Delta R/R_0$ of MoS_2/NH is negative and has a relatively large magnitude (Figure 2b). These results suggest that a large portion of incoming long-wavelength light should be absorbed at the near-hole-edge region of MoS_2/NH. The density of photo-generated excitons is proportional to the intensity of incident light at the MoS_2 monolayers.[23] Thus, the optical simulation results in Figure 6 should be considered to understand the SPV spectra in Figure 5.

Figure 7 illustrates how photo-generated charge carriers affect the distinct features of the measured SPV spectra in Figure 5. The CPD_D maps (Figure 1c,d) show the electric potential (V) distributions of MoS_2/ND and MoS_2/NH, as schematically illustrated in the top of Figure 7. The gradient of V drives separation of excitons and drift of charge carriers, as discussed above. The resulting spatial distribution of charges should affect the CPD_L. In-plane movement of charges are considered in Figure 7 because out-of-plane motion of charges is impossible in atomically thin MoS_2 monolayers. In MoS_2/ND, the optical simulation results in Figure 6 suggest that a relatively large number of excitons are created at the MoS_2 region on the SiO_2 surface under illumination by short-wavelength light. The potential gradient around the Au NDs causes separation of the photo-generated excitons and drift of electrons away from the Au NDs, as illustrated in Figure 7. The resulting negative charging of the MoS_2 region on the SiO_2 surface causes CPD_L to decrease compared with CPD_D, resulting in a positive SPV. At longer wavelengths, hot spots appear (Figure 6) that create more excitons near the Au NDs. Thus, the contribution of the MoS_2/Au region is important for determining the overall long-wavelength SPV of MoS_2/NDs despite the small area fraction of the whole sample surface. Because MoS_2 monolayers on Au thin films have small SPV signals (Figure S3, Supporting Information), the magnitude of the measured SPV was reduced at long wavelengths (Figure 5).

In MoS_2/NH, illumination of short-wavelength light produced many excitons in the suspended MoS_2 region, owing to the strong light intensity (Figure 6). From the V distribution in the MoS_2/NH (Figure 7b), electrons are supposed to move toward the Au layer. The depletion of photo-generated electrons induced positive charging of the suspended MoS_2 region, leading to a negative SPV signal (i.e., $CPD_D < CPD_L$). At longer wavelengths, the local density of photo-generated excitons near the Au NH edges increased because of the strong light confinement (Figure 6). This effect decreased the number of net charges in the suspended MoS_2 region and the magnitude of the measured SPV.

The interfacial band alignment allows charge transfer at the MoS_2/Au contacts, which was considered to explain the CPD maps (Figure 1) and the PL quenching results (Figure 4).[6,13] Au thin films have a large number of free electrons, hence the Au nanopatterns in both ND and NH can act as charge reservoirs. As a result, the MoS_2 region in contact with the Au layer cannot show a large SPV signal, as shown in Figure S3. KPFM-measured CPD mappings of the samples also show the relatively small CPD changes at the MoS_2/Au contact region under illumination of a 635 nm wavelength laser diode (Figure S4, Supporting Information). Thus, the averaged SPV signals of both the MoS_2/ND and MoS_2/NH depend on the area fraction of the MoS_2/SiO_2 region. Moreover, the spatial distributions of light intensity and resulting photo-generated excitons play an important role in understanding the SPV spectra in Figure 5. Complementary studies of the optical and SPV characteristics of MoS_2/ND and MoS_2/NH allow us to explain photon−plasmon−exciton coupling behaviors in the hybrid nanostructures.

CONCLUSIONS

MoS_2/ND and MoS_2/NH hybrid nanostructures were fabricated using NSL and exfoliation-transfer techniques. Angle-resolved reflectance spectra of MoS_2/ND and MoS_2/NH clearly indicated excitation of LSPs and SPPs. The LSP- and SPP-exciton coupling in these hybrid nanostructures enhanced the PL intensity of the MoS_2 monolayers. Notably, the SPV data revealed the opposite polarity of the excess photo-generated charges in MoS_2, that is, negative and positive charging in MoS_2/ND and MoS_2/NH, respectively. This distinct SPV polarity is attributed to the electric potential

https://dx.doi.org/10.1021/acsami.0c14563
ACS Appl. Mater. Interfaces XXXX, XXX, XXX−XXX

distributions in MoS_2/ND and MoS_2/NH. Furthermore, the local density of the photo-generated excitons, extrapolated from the finite difference time domain simulations, allowed us to explain the SPV spectra. This work shows that properly designed plasmonic nanostructures enable control over the spatial distribution of photo-generated carriers in MoS_2/metal hybrid nanostructures.

METHODS

Sample Fabrication. The two kinds of Au nanopatterns, ND array and NH array, were fabricated on SiO_2(100 nm)/Si wafers using the NSL technique. Monolayers of a hexagonal PS bead array (diameter: 520 nm) were prepared on the wafers. Then, 50 nm Au thin films with 3 nm Ti adhesion layers were deposited on the PS-coated wafers by electron-beam evaporation, and the ND pattern was obtained after removal of PS beads. To make the NH pattern, the diameter of the PS beads was reduced to 400 nm by reactive ion etching. The Au(50 nm)/Ti(3 nm) thin films were deposited on the etched loose-packed PS bead monolayer. MoS_2 monolayer flakes, whose typical size is 10−20 μm, were grown by chemical vapor deposition on Si substrates with 300 nm-thick SiO_2 layers.[22] The MoS_2 monolayer flakes were then transferred onto the ND and NH patterns by a wet-transfer method.

KPFM Measurements. The surface topography and CPD maps were obtained by an AFM system (NX-10, Park Systems) with a glovebox. All measurements were carried out in a N_2 atmosphere to avoid artifacts caused by the ambient gas adsorption. Pt/Ir-coated Si cantilevers were used as the tip, and its work function was calibrated against a highly ordered pyrolytic graphite (SPI Suppliers) reference sample. A near-infrared laser diode (wavelength: 930 nm) was used to detect the deflection of the cantilever. The presence of MoS_2 flakes was confirmed from the CPD data (Figure S1, Supporting Information).

Macroscopic Reflectance Measurements. Specular reflectance spectra were measured with the use of a quantum efficiency measurement system (QuantX-300, Newport). A xenon arc lamp and a monochromator were used to generate monochromatic light in the range of 400−800 nm, where the beam size was approximately 1 mm^2. A high−low reflectance standard (product number: 603414) was used for calibration before measurements. After calibration, the samples were sequentially mounted on the sample stage and the reflectance spectrum of each sample was measured with the use of QuantX software during measurements.

Angle-Resolved Micro-Reflectance and PL Measurements. Angle-resolved micro-reflectance spectra were collected using a home-built angle-resolved microscopy setup. White light was focused onto the sample by a 60× microscope objective (numerical aperture NA = 0.7), and the focused beam size is ∼10 μm. In the angle-resolved reflectance measurements, the back focal plane of the objective lens was projected to the entrance slit of a spectrometer equipped with a charge-coupled device detector (Princeton Instruments, 512 × 2048 pixels) by a set of lenses. PL spectra were collected using the same home-built microscopy setup, and the beam diameter was 1.0 μm. As an excitation source, an argon-ion laser at 457.9 nm (continuous wave) was focused through the objective lens, and the signal through the same objective was collected by an optical fiber, which was coupled to the spectrometer.

SPV Spectroscopy Measurements. SPV signals were measured in air with a scanning Kelvin probe apparatus (SKP5050, KP Technology) using a 2 mm diameter vibrating probe (frequency = 67 Hz). The tungsten lamp illumination was from the top side of the sample. The SPV spectra were measured with continuous monochromatic light at wavelengths in the range from 800 to 400 nm, selected using a linear variable filter.

ASSOCIATED CONTENT

Supporting Information

The Supporting Information is available free of charge at https://pubs.acs.org/doi/10.1021/acsami.0c14563.

AFM images, contact potential in dark maps, and height profiles of MoS_2/ND and MoS_2/NH; optical reflectance spectra of a bare SiO_2/Si substrate, 50 nm Au-coated SiO_2/Si substrate, bare Au ND, and bare NH; SPV spectra of a bare SiO_2/Si substrate, MoS_2 flakes on a bare SiO_2/Si substrate, and MoS_2 flakes on a 50 nm Au-coated SiO_2/Si substrate; and KPFM-measured CPD mappings of the bare Au ND, MoS_2/ND, bare NH, and MoS_2/NH samples in dark and under illumination (PDF)

AUTHOR INFORMATION

Corresponding Author

Dong-Wook Kim − *Department of Physics, Ewha Womans University, Seoul 03760, Korea;* orcid.org/0000-0002-5687-7739; Email: dwkim@ewha.ac.kr

Authors

Jungeun Song − *Department of Physics, Ewha Womans University, Seoul 03760, Korea*

Soyeong Kwon − *Department of Physics, Ewha Womans University, Seoul 03760, Korea*

Bora Kim − *Department of Physics, Ewha Womans University, Seoul 03760, Korea*

Eunah Kim − *Department of Energy Science, Sungkyunkwan University, Suwon 16419, Korea*

Lakshmi N. S. Murthy − *Department of Materials Science and Engineering, University of Texas at Dallas, Richardson, Texas 75080, United States*

Taejin Lee − *Department of Emerging Materials Science, Daegu Gyeongbuk Institute of Science and Technology (DGIST), Daegu 42988, Korea*

Inhae Hong − *Division of Chemical Engineering and Materials Science, Ewha Womans University, Seoul 03760, Korea*

Byoung Hoon Lee − *Division of Chemical Engineering and Materials Science, Ewha Womans University, Seoul 03760, Korea;* orcid.org/0000-0001-5176-9838

Sang Wook Lee − *Department of Physics, Ewha Womans University, Seoul 03760, Korea;* orcid.org/0000-0003-2265-4761

Soo Ho Choi − *Center for Integrated Nanostructure Physics (CINAP), Institute of Basic Science (IBS), Sungkyunkwan University, Suwon 16419, Korea;* orcid.org/0000-0002-9927-0101

Ki Kang Kim − *Department of Energy Science and Center for Integrated Nanostructure Physics (CINAP), Institute of Basic Science (IBS), Sungkyunkwan University, Suwon 16419, Korea;* orcid.org/0000-0003-1008-6744

Chang-Hee Cho − *Department of Emerging Materials Science, Daegu Gyeongbuk Institute of Science and Technology (DGIST), Daegu 42988, Korea;* orcid.org/0000-0003-0014-5464

Julia W. P. Hsu − *Department of Materials Science and Engineering, University of Texas at Dallas, Richardson, Texas 75080, United States;* orcid.org/0000-0002-7821-3001

Complete contact information is available at: https://pubs.acs.org/10.1021/acsami.0c14563

https://dx.doi.org/10.1021/acsami.0c14563
ACS Appl. Mater. Interfaces XXXX, XXX, XXX−XXX

Notes

The authors declare no competing financial interest.

■ ACKNOWLEDGMENTS

This work was supported by a National Research Foundation of Korea Grant (2018K1A4A3A01064272, 2019R1A2C1006772, and 2019R1A4A1029052) and the DGIST Basic Research Program (grant number: 20-CoE-NT-01), funded by the Ministry of Science and ICT of the Korean Government. L.N.S.M. and J.W.P.H. acknowledge the support of the National Science Foundation (CBET-1916612). J.W.P.H. also acknowledges the Texas Instruments Distinguished Chair in Nanoelectronics.

■ REFERENCES

(1) Jariwala, D.; Davoyan, A. R.; Wong, J.; Atwater, H. A. van der Waals Materials for Atomically-Thin Photovoltaics: Promise and Outlook. *ACS Photonics* **2017**, *4*, 2962−2970.

(2) Yang, X.; Yu, H.; Guo, X.; Ding, Q.; Pullerits, T.; Wang, R.; Zhang, G.; Liang, W.; Sun, M. Plasmon-Exciton Coupling of Monolayer MoS_2-Ag Nanoparticles Hybrids for Surface Catalytic Reaction. *Mater. Today Energy* **2017**, *5*, 72−78.

(3) Cheng, J.; Wang, C.; Zou, X.; Liao, L. Recent Advances in Optoelectronic Devices Based on 2D Materials and Their Heterostructures. *Adv. Opt. Mater.* **2019**, *7*, 1800441.

(4) Najmaei, S.; Mlayah, A.; Arbouet, A.; Girard, C.; Léotin, J.; Lou, J. Plasmonic Pumping of Excitonic Photoluminescence in Hybrid MoS_2-Au Nanostructures. *ACS Photonics* **2014**, *8*, 12682−12689.

(5) Butun, S.; Tongay, S.; Aydin, K. Enhanced Light Emission from Large-Area Monolayer MoS_2 Using Plasmonic Nanodisc Arrays. *Nano Lett.* **2015**, *15*, 2700−2704.

(6) Yan, J.; Ma, C.; Liu, P.; Yang, G. Plasmon-Induced Energy Transfer and Photoluminescnce Manipulation in MoS_2 with a Different Number of Layers. *ACS Photonics* **2017**, *4*, 1092−1100.

(7) Bang, S.; Duong, N. T.; Lee, J.; Cho, Y. H.; Oh, H. M.; Kim, H.; Yun, S. J.; Park, C.; Kwon, M.-K.; Kim, J.-Y.; Kim, J.; Jeong, M. S. Augmented Quantum Yield of a 2D Monolayer Photodetector by Surface Plasmon Coupling. *Nano Lett.* **2018**, *18*, 2316−2323.

(8) Lee, H. S.; Kim, M. S.; Jin, Y.; Han, G. H.; Lee, Y. H.; Kim, J. Selective Amplification of the Primary Exciton in a MoS_2 Monolayer. *Phys. Rev. Lett.* **2015**, *115*, 226801.

(9) Liu, W.; Lee, B.; Naylor, C. H.; Ee, H.-S.; Park, J.; Johnson, A. T. C.; Agarwal, R. Strong Exciton−Plasmon Coupling in MoS_2 Coupled with Plasmonic Lattice. *Nano Lett.* **2016**, *16*, 1262−1269.

(10) Shan, H.; Yu, Y.; Wang, X.; Luo, Y.; Zu, S.; Du, B.; Han, T.; Li, B.; Li, Y.; Wu, J.; Lin, F.; Shi, K.; Tay, B. K.; Liu, Z.; Zhu, X.; Fang, Z. Direct Observation of Ultrafast Plasmonic Hot Electron Transfer in the Strong Coupling Regime. *Light: Sci. Appl.* **2019**, *8*, 9.

(11) Hernandez, R.; Juliano Martins, R.; Agreda, A.; Petit, M.; Weeber, J.-C.; Bouhelier, A.; Cluzel, B.; Demichel, O. Delocalized Hot Electron Generation with Propagative Surface Plasmon Polaritons. *ACS Photonics* **2019**, *6*, 1500−1505.

(12) Rahaman, M.; Rodriguez, R. D.; Plechinger, G.; Moras, S.; Schüller, C.; Korn, T.; Zahn, D. R. T. Highly Localized Strain in a MoS_2/Au Heterostructure Revealed by Tip-Enhanced Raman Spectroscopy. *Nano Lett.* **2017**, *17*, 6027−6033.

(13) Sohn, A.; Moon, H.; Kim, J.; Seo, M.; Min, K.-A.; Lee, S. W.; Yoon, S.; Hong, S.; Kim, D.-W. Band Alignment at Au/MoS_2 Contacts: Thickness Dependence of Exfoliated Flakes. *J. Phys. Chem. C* **2017**, *121*, 22517−22522.

(14) Jensen, T. R.; Schatz, G. C.; Van Duyne, R. P. Nanosphere Lithography: Surface Plasmon Resonance Spectrum of a Periodic Array of Silver Nanoparticles by Ultraviolet-Visible Extinction Spectroscopy and Electrodynamic Modeling. *J. Phys. Chem. B* **1999**, *103*, 2394−2401.

(15) Murray, W. A.; Astilean, S.; Barnes, W. L. Transition from Localized Surface Plasmon Resonance to Extended Surface Plasmon-Polariton as Metallic Nanoparticles Merge to Form a Periodic Hole Array. *Phys. Rev. B: Condens. Matter Mater. Phys.* **2004**, *69*, 165407.

(16) Lee, S. H.; Bantz, K. C.; Lindquist, N. C.; Oh, S.-H.; Haynes, C. L. Self-Assembled Plasmonic Nanohole Arrays. *Langmuir* **2009**, *25*, 13685−13693.

(17) Petronijevic, E.; Belardini, A.; Leahu, G.; Cesca, T.; Scian, C.; Mattei, G.; Sibilia, C. Circular Dichroism in Low-Cost Plasmonics: 2D Arrays of Nanoholes in Silver. *Appl. Sci.* **2020**, *10*, 1316.

(18) Zerweck, U.; Loppacher, C.; Otto, T.; Grafström, S.; Eng, L. M. Accuracy and Resolution Limits of Kelvin Probe Force Microscopy. *Phys. Rev. B: Condens. Matter Mater. Phys.* **2005**, *71*, 125424.

(19) Kronik, L.; Shapira, Y. Surface Photovoltage Phenomena: Theory, Experiment, and Applications. *Surf. Sci. Rep.* **1999**, *37*, 1−206.

(20) Lee, Y.-J.; Wang, J.; Hsu, J. W. P. Surface Phovoltage Characterization of Organic Photovoltiac Devices. *Appl. Phys. Lett.* **2013**, *103*, 173302.

(21) Murthy, L. N. S.; Barrera, D.; Xu, L.; Gadh, A.; Cao, F.-Y.; Tseng, C.-C.; Cheng, Y.-J.; Hsu, J. W. P. Probing Defect States in Organic Polymers and Bulk Heterojunctions Using Surface Photovoltage Spectroscopy. *J. Phys. Chem. C* **2019**, *123*, 10795−10801.

(22) Boandoh, S.; Choi, S. H.; Park, J.-H.; Park, S. Y.; Bang, S.; Jeong, M. S.; Lee, J. S.; Kim, H. J.; Yang, W.; Choi, J.-Y.; Kim, S. M.; Kim, K. K. A Novel and Facile Route to Synthesize Atomic-Layered MoS_2 Film for Large-Area Electronics. *Small* **2017**, *13*, 1701306.

(23) Kim, E.; Cho, J.-W.; Kim, B. R.; Nguyen, T. T. T.; Nam, Y.-H.; Kim, S.-K.; Yoon, S.; Kim, Y. S.; Lee, J.-H.; Kim, D.-W. Interference-Enhanced Broadband Absorption of Monolayer MoS_2 on Sub-100 nm Thick SiO_2/Si Substrates: Reflection and Transmission Phase Changes at Interfaces. *Adv. Mater. Interfaces* **2018**, *5*, 1701637.

(24) Buscema, M.; Steele, G. A.; van der Zant, H. S. J.; Castellanos-Gomez, A. The Effect of the Substrate on the Raman and Photoluminescence Emission of Single-Layer MoS_2. *Nano Res.* **2014**, *7*, 561−571.

(25) Kang, J.-W.; Song, B.; Liu, W.; Park, S.-J.; Agarwal, R.; Cho, C.-H. Room Temperature Polariton Lasing in Quantum Heterostructg-ure Nanovacities. *Sci. Adv.* **2019**, *5*, No. eaau9338.

(26) Steinert, C.; Tengeler, S.; Kaiser, B.; Jaegermann, W. The Impact of Different Si Surface Terminations in the (100) p-Si^{ln+}-Sil Cu Junction with Respect to the Photo Electrochemical Performance. *J. Electrochem. Soc.* **2019**, *166*, H3208.

(27) Palik, E. D. *Handbook of Optical Constants of Solids*; Academic Press: San Diego, CA, 1985.

(28) Lide, D. R. *Handbook of Chemistry and Physics*, 76th ed.; CRC Press; Boca Raton, FL, 1995.

(29) Correia-Ledo, D.; Gibson, K. F.; Dhawan, A.; Couture, M.; Vo-Dinh, T.; Graham, D.; Masson, J.-F. Assessing the Location of Surface Plasmons Over Nanotriangle and Nanohole Arrays of Different Size and Periodicity. *J. Phys. Chem. C* **2012**, *116*, 6884−6892.

(30) García-Vidal, F. J.; Pendry, J. B. Collective Theory for Surface Enhanced Raman Scattering. *Phys. Rev. Lett.* **1996**, *77*, 1163−1166.

https://dx.doi.org/10.1021/acsami.0c14563
ACS Appl. Mater. Interfaces XXXX, XXX, XXX−XXX